Impact of a Heated Wall on the Laminar-to-Turbulent Transition of Crossflow Vortices an Experimental Study

Barahona Lopez, M.; van de Weijer, A.F.; Rius Vidales, A.F.; Kotsonis, M.

Important note
To cite this publication, please use the final published version (if applicable).
Please check the document version above.

Impact of a Heated Wall on the Laminar-to-Turbulent Transition of Crossflow Vortices: an Experimental Study

Marina Barahona*, Tim A. F. van de Weijer†, Alberto F. Rius-Vidales‡, and Marios Kotsonis§

Delft University of Technology, Kluyverweg 1, 2629HS Delft, The Netherlands

One of the most critical technological challenges embedded in the electrification of future aircraft revolves around the thermal management of batteries and fuel cells. An innovative idea involves using the aircraft's aerodynamic surfaces to dissipate the extra heat, thereby reducing the impact that traditional thermal management systems (e.g. ram air heat exchanger) have on the overall aerodynamic efficiency of the aircraft. However, the limited experimental research addressing the influence of a heated surface on the stability and transition of the crossflow instability (CFI) hinders the assessment of the aerodynamic impact of this technology for future aircraft, where swept wings are ubiquitous. Thus, the objective of this work is to experimentally study the effect of a heated wall on the stability and final breakdown of CF vortices. To do so, experiments are conducted on a 45° swept flat plate wind tunnel model, where the surface temperature is increased by means of a surface-embedded electrical heater, yielding a mean wall-temperature ratio of $T_w/T_\infty = 1.055$. Overall, the experimental (i.e. HWA) and numerical (i.e. CLST) results show that wall heating leads to significant destabilization of the stationary CFI. Interestingly, a spectral analysis of the HWA signal reveals substantial amplification of the traveling CF mode under wall-heating conditions, which in turn appears significantly more destabilized than the stationary CF mode. Additionally, inspection of the high-frequency content in the HWA measurements indicates premature breakdown of the CF vortices and advancement of the laminar-turbulent transition by $\Delta x/c_x = 6.3\%$ with wall heating. The results presented in this work render a first insight into the impact of a non-adiabatic wall on the development of the crossflow instability and subsequent breakdown to turbulence.

Nomenclature

A	=	disturbance amplitude integrated in wall-normal direction [m/s]
a_{rms}	=	in-plane integral of r.m.s velocity fluctuations [m/s]
C_p	=	pressure coefficient, $C_p = (P_{\text{static}} - P_{\text{total}})/(1/2\rho_0 U_0^2)$
Λ	=	sweep angle [deg]
h_x	=	local heat transfer coefficient [W/m^{2}K]
P	=	power spectral density [(m/s)^2/Hz]
Q	=	velocity detected at the hot-wire [m/s]
T_w	=	wall temperature [degC]
T_∞	=	freestream temperature [degC]
T_0	=	reference temperature in numerical setup [degC]
X, Y, Z	=	wind tunnel oriented coordinate system [m]
x, y, z	=	leading edge oriented coordinate system [m]
σ_Q	=	root mean square (r.m.s) of the velocity fluctuations [m/s]
β_H	=	Hartree parameter

*PhD Candidate, Department of Flow Physics and Technology, Faculty of Aerospace Engineering, M.BarahonaLopez@tudelft.nl

†MSc Student, Department of Flow Physics and Technology, Faculty of Aerospace Engineering, A.F.vandeweijer@student.tudelft.nl

‡Post-Doctoral Researcher, Department of Flow Physics and Technology, Faculty of Aerospace Engineering, A.F.RiusVidales@tudelft.nl

§Full Professor, Department of Flow Physics and Technology, Faculty of Aerospace Engineering, M.Kotsonis@tudelft.nl

I. Introduction

THE ambitious environmental goals outlined in the FlightPath 2050 document require the implementation of revolutionary technological changes in future aircraft. At present, a promising concept to reduce the aviation emissions involves the full or partial electrification of the propulsion system using batteries or fuel cells. Unfortunately, the onboard integration of these electric-based propulsion systems gives rise to additional technological challenges. One major obstacle concerns the high heat loads generated by batteries and fuel cells [1]. In contrast to traditional turbofan engines, where large part of the heat generated is rejected naturally through the engine gas exhaust, these electrical components can only dissipate heat through conduction [2]. In addition, for the most technologically mature Proton-Exchange Membrane Fuel Cells (PEMFC), heat generation occurs at relatively low operating temperatures, i.e. 90-95 degC [3]. Therefore, the optimal integration of electrical propulsion systems into future aircraft necessitates efficient Thermal Management Systems (TMS), capable of dissipating the additional heat generated by the electrical components without significantly compromising the aircraft's performance.

Ram-air duct heat exchangers, owing to their simplicity, effectiveness, and integration in operational aircraft, stand as the most mature technology among Thermal Management Systems (TMS). Nevertheless, a notable drawback of ram-air TMS is the consequential increase in weight and cooling drag [4]. An innovative alternative to ram-air heat exchangers involves using the outer aircraft skin for heat dissipation, known as Outer Mold Line (OML) cooling [5]. The use of OML systems can lower weight and drag penalties due to the reduced number of components required and the absence of aerodynamic modifications to the aircraft surfaces. Several aircraft-level analyses [4, 5] have already showcased the feasibility of this technology to efficiently cool-down the powertrain components of different electrified aircraft concepts.

Recently, the aerodynamic impact of heating the aircraft skin has been investigated in more detail by Habermann et al. [6]. The authors used RANS CFD simulations to study the influence of heat rejection on the turbulent boundary layer developing over the wing of a turboprop aircraft. Their findings indicate that the lift-to-drag ratio of the aircraft decreases by 4% with this technology. Nevertheless, the influence of this technology on the laminar and transitional flow regimes was not addressed in their study.

The leading edge (LE) of an aircraft constitutes one of the most effective areas for heat dissipation [5]. The rapid acceleration experienced by the flow at the LE significantly enhances the transfer of heat between the aircraft's skin and the surrounding air. However, due to the laminar state of the boundary layer in this region, the presence of a heated surface can potentially change the laminar-to-turbulent transition location, thereby modifying the skin friction drag. Nevertheless, limited research has been conducted to investigate the impact of OML cooling on laminar-to-turbulent transition.

Within the boundary layer, the existence of a relatively hot skin increases the fluid's near-wall viscosity, leading to a higher momentum deficit. Under these conditions, boundary layer instabilities are more effectively amplified. In configurations featuring unswept wings, laminar-to-turbulent transition is primarily governed by Tollmien-Schlichting waves, while Crossflow Instabilities (CFI) dominate the transition process in swept wings. The impact of a non-adiabatic wall has been observed to be different for these two instabilities.

Previous research on thermal control of boundary layer instabilities focused on uniform wall-cooling and localized heating to stabilize TS-dominated transition scenarios. Several authors have previously demonstrated through experiments [7, 8] and linear stability theory [9, 10] that the spatial growth of Tollmien-Schlichting (TS) waves is significantly affected by the presence of a non-adiabatic wall. Leveraging the stabilizing effect of wall-cooling on TS waves, Dovgal et al. [11] applied localized heating to achieve stabilization downstream of the heating strip, where the flow encounters a relatively cooler surface. Subsequent stability analyses and DNS results performed by Masad [12] and Kral et al. [13], respectively, confirmed that significant stabilization of TS waves can be achieved by placing a heating strip upstream or close to branch I, in a region where TS waves are stable.

Inspired by the substantial impact of thermal control on TS-dominated transition scenarios, other studies have explored this strategy on CFI, crucial to describe the laminar-to-turbulent transition in swept wings. Linear Stability Theory (LST) results presented in [14], [10], and [15] have indicated that CFI are stabilized by wall-cooling and destabilized by wall-heating. However, the work of Lekoudis [10] highlights that the stabilization achieved with wall-cooling for CFI is significantly weaker than the one attained with TS waves. Similar conclusions were drawn from the stability results of Bertolotti and Bieler [16], where a cooling strip was applied in the unstable region of both TS waves and CFI, revealing a more significant stabilization of the former with respect to the latter. Additionally, the stability results presented in Ren and Kloker [15] suggest that traveling crossflow modes are more sensitive to modifications of the wall temperature than the stationary CFI. Similar findings to Ren and Kloker [15] have also been observed in the experimental work of Eppink and Wlezien [17] where, by applying a mild cooled surface over a 35-degree swept wing

2

model, the authors report significant stabilization of traveling CFI compared to the stationary CF mode.

Previous experimental studies on the effect of non-adiabatic walls on stationary CFI have been conducted as a secondary effect of Temperature Sensitive Paint (TSP) measurements. One example of this is the work of Lemarechal et al. [18], where TSP is applied on a swept wing model and the effect of wall-temperature is investigated to determine a permissible wall-temperature ratio that does not affect laminar-to-turbulent transition, found to be $T_w/T_\infty = 1.04$. However, TSP measurements conducted in the European Transonic Wind Tunnel (ETW) by Fey et al. [19] on a swept wing model under larger wall-temperature variations ($T_w/T_\infty \leq 0.93$) show a considerable influence on the transition behaviour.

The aforementioned works suggest that crossflow instabilities are weakly affected by a non-adiabatic wall compared to TS waves. Some authors [20] attribute these differences to the inflectional nature of CFI compared to the viscous nature of TS waves, the latter being more sensitive to near-wall viscosity modifications. However, the lack of dedicated experimental and numerical studies examining the development of CF vortices (linear and non-linear regime) in the presence of non-adiabatic walls hinders the validation of these propositions and challenges the problem understanding. This limitation, in turn, may pose challenges for subsequent studies aiming to evaluate the potential drag penalty of using the leading edge as a heat rejection region in swept wings. In light of this, the present work aims to experimentally study the effect of a heated wall on the stability and breakdown of stationary CF vortices.

The structure of this document is as follows. In Sec. II the numerical and experimental setup employed are explained in-detail. The nomenclature and different metrics used to present this work's results are introduced at the end of Sec. II. Sec. III.A analyzes the differences observed from the time-averaged flow under adiabatic and wall-heating conditions. The amplification of the steady perturbation content in the presence of wall-heating is studied in Sec. III.B, where the evolution of the forced crossflow mode and its higher harmonics is analyzed. Sec. III.C examines the influence of wall-heating on the development of secondary CFI and the laminar-to-turbulent transition and Sec. III.D investigates the laminar breakdown under wall-heating and adiabatic conditions. Finally, Sec. IV outlines the main conclusions drawn from this work's results.

II. Methodology

A. Experimental setup

The experiments presented herein are conducted at the A-tunnel, a low-turbulence, open-jet, subsonic, vertical wind tunnel located at the Delft University of Technology [21]. At the flow conditions of this work and in the presence of the test model, the turbulence intensity levels are: $T_u = (1/U_\infty)\sqrt{(1/2)(u'^2 + v'^2)} \le 0.06\%$, band-pass filtered between $5 \le f_{BP} \le 2 \times 10^4$ Hz [22]. The low turbulence intensity levels achieved enable the study of transition driven by stationary CFI.

The freestream ambient temperature (T_∞) and pressure (P_∞) are monitored by means of a Resistance Temperature Detector (RTD-Pt100)* and a digital barometer†, respectively. From these values, the freestream air density (ρ_∞) and viscosity (ν_∞) are calculated to determine the Reynolds number as $Re_{c_X} = U_\infty c_X/\nu_\infty$, where c_X is the chord length. The velocity at the nozzle outlet is determined as $U_\infty = \sqrt{2q_\infty/\rho}$ using the difference‡ between the total and static pressure (dynamic pressure, $q_\infty = P_t - P_s$) measured at a pitot static tube located 0.5 m upstream of the model's LE. The mean experimental freestream conditions over the different measurement cases are specified in Table 1.

An aluminum swept flat plate model of 20 mm thickness and $45°$ of sweep is used for these experiments, as illustrated in Fig. 1. This model is denoted as Swept Transition Experimental Platform or STEP in what follows §. The model features two separate segments from $0 \le x/c_X \le 0.397$ (upstream plate) and $0.397 \le x/c_X \le 0.603$ (downstream plate). Both plates can move independent of each other, enabling the generation of backward-facing and forward-facing step discontinuities in the model surface. Nevertheless, this feature is not used during these experiments.
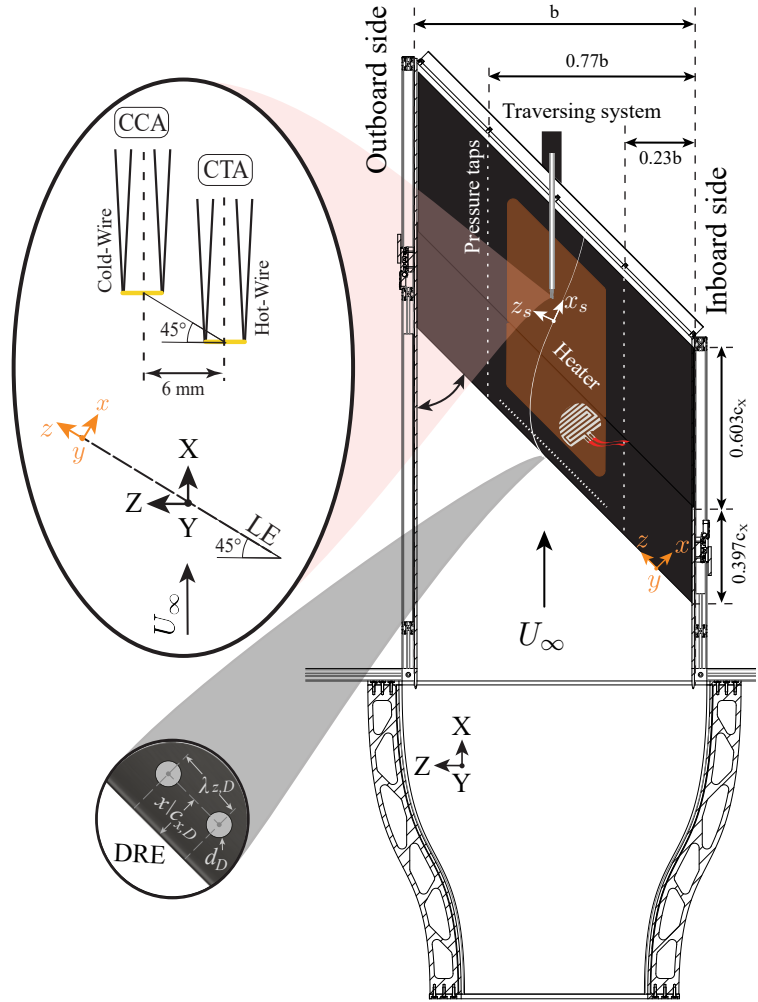
A nozzle is used to adapt the circular inlet

Fig. 1 Schematic of the STEP model geometry and main components (C-HWA, DREs, pressure taps and heating elements). The model features a chord length of $c_X = 0.848$ m and a span of $b = 0.884$ m. The orange pad on the model surface represents the area where the silicon heaters are placed. Sketch dimensions do not represent the real-scale model dimensions.

at the plenum of diameter 600 mm to the rectangular test section with dimensions 250×1000 mm. Two different coordinate systems are distinguished: a global set of coordinates (X,Y,Z) aligned with the test section horizontal axis and a local set of coordinates (x,y,z) aligned with the model's LE (note the axis indicated in Fig. 1). The model features a Modified Super Ellipse (MSE) geometry at the LE [24] with aspect ratio AR = 6 and surface roughness of $R_q \approx 0.6$ μm. The location of the stagnation point and the LE pressure distribution is adjusted with a 5 cm trailing edge

---

*Platinum resistance temperature detector (Pt100), 1/3 DIN (± 0.1 degC at 20 degC).

†Barometer by Amphenol (amphenol-sensors.com), model: NPA-201, accuracy 0.01% of reading.

‡Differential pressure sensor by Honeywell (sps.honeywell.com), model: RSC-005ND, range ±1246 Pa, accuracy ±13 Pa.

§Further details on the features of this model can be found in the PhD Dissertation of A. F. Rius-Vidales [23].

4

(TE) flap deflected approximately 18.16° upwards (towards the measurement region) during the experiments. The flow on the back of the flat plate is tripped by means of zig-zag tape to avoid undesired shedding at the TE.

The geometry of the top wall can be adjusted using eight linear actuators to achieve a target pressure distribution over the model. Two rows of 63 static pressure taps (126 in total) located at the outboard and inboard side of the model, as indicated in Fig. 1, measure the pressure distribution imposed by the top wall using a set of differential pressure transducers¶. The experimental pressure distribution measured by outboard and inboard pressure taps is shown in Fig. 2, depicting a linearly decreasing static pressure within the measurement region (i.e. favorable pressure gradient). The overlap between inboard and outboard pressure measurements confirms the validity of spanwise invariant flow assumption used throughout the numerical methodology.

Parameter	U_∞	P_∞	T_∞	Re_{c_X}
Value	15.73 m/s	1.015 bar	26 degC	8.56×10^5

Table 1   Freestream conditions.

The spanwise wavelength of the CFI modes is conditioned using Discrete Roughness Elements (DREs), following the success of this procedure reported in previous experimental works [25–27]. The DREs are manufactured from adhesive vinyl foil using a CNC cutter, where the thickness of the DREs (k_D) is determined by the thickness of the film, while the spacing (λ_z) and diameter of the elements (d_D) are customized. The spanwise spacing and location (s_D) of the DREs are selected to match the wavelength and neutral point of the most amplified (primary) stationary CFI mode, respectively. The latter quantities are determined from the solution of the Compressible Linear Stability (CLST) solver for the experimentally measured pressure distribution (refer to Sec. II.C). The remaining DREs parameters (thickness and diameter) are carefully chosen in accordance to previous studies (e.g. [28]) to ensure linear receptivity. Table 2 presents the DREs location and geometrical parameters employed in the experiments.

Parameter	λ_D	d_D	k_D	s_D/c_x
Value	10 mm	2 mm	125 mm	0.103

Table 2   DREs geometrical parameters.

The back of the upstream and downstream plates of the STEP model feature two inserts where active heating devices are placed (see Fig. 1). Wall-heating is realized by means of two temperature-controlled and custom-made silicon heaters‖ with different electrical powers of 200 W (upstream plate) and 400 W (downstream plate). The maximum temperature attained by the thermal pads is 50 degC.

The performance of the heating devices is evaluated numerically using COMSOL Multiphysics heat transfer module. The objective is to reproduce the temperature distribution on the measurement side and establish the wall boundary condition for the compressible baseflow calculation. The boundary conditions in the thermal simulations are set in accordance to the experimental conditions. On the backside of the model, the heaters are insulated, while the remaining surface is exposed to forced convection by turbulent flow. Convection over the measurement side is set to match the streamwise dependence of the heat transfer coefficient, $h(x)$, from the CBL boundary layer solution at the conditions of the experiments. The heat flux delivered by the heaters is adjusted until convergence between the temperature distribution over the measurement surface and the wall temperature measured during the experiments is reached, note Fig. 2.

The temperature over the measurement surface is continuously monitored by means of surface-embedded Type-K thermocouples and an Infrared (IR) camera**. These measurements enable further validation of the COMSOL simulation framework utilized herein for obtaining the wall temperature distribution.

¶Custom-made pressure scanner (NUB-System) with Honeywell HSC series differential pressure transducers with ranges ±160, ±600, and ±2488 Pa with accuracy ±6, ±9 and ±25 Pa.

‖Custom-made silicon heaters manufactured by the company Kracht (kracht.nl).

**Optris PI640 IR camera with sensor size of 640pixel×480pixel, uncooled focal plane array, 7.5–13 μm spectral range, NETID 75 mK.
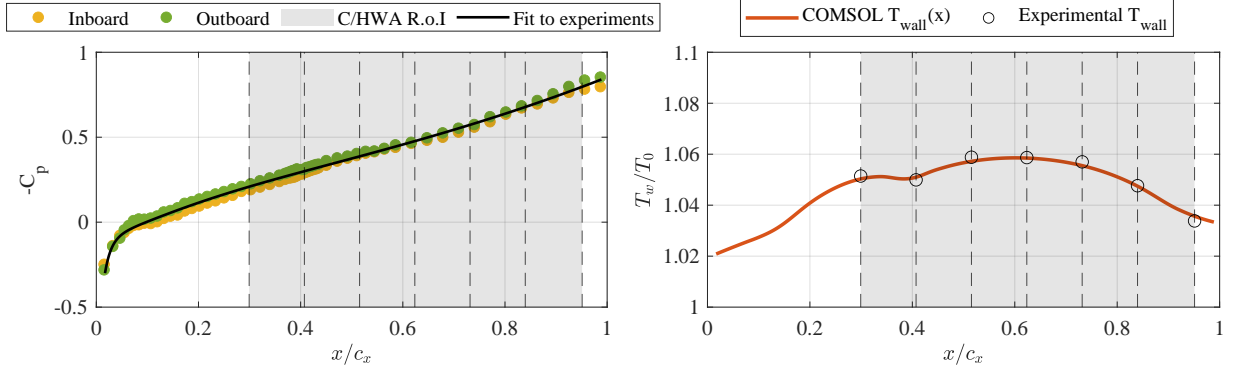
Fig. 2 Input parameters for CBL and CLST solver. Pressure coefficient from pressure taps measurements (left) and wall temperature distribution from COMSOL simulations and experiments (right).

B. Hot-wire and cold-wire anemometry

Hot-Wire Anemometry (HWA) is used to inspect the boundary layer during these experiments. However, given the imposed temperature difference between the wall and the freestream, it is of major importance to also retrieve the spatial temperature distribution, necessary to locally correct the HWA in-situ calibration and determine the flow velocity. In addition, evaluating the thermal field will yield valuable insights into other flow features that can contribute to a better understanding of the problem. For instance, it can shed light on the the modulation that the CF vortices impart on the thermal boundary layer. For this purpose, a cold-wire is used to retrieve the temperature field.

It is well-known that hot-wires are also sensitive to temperature changes. The sensitivity of hot-wires in Constant Current Anemometry (CCA) mode to velocity versus temperature can be described as follows [29]:

$$\frac{S_T}{S_U} \sim -2\left(A + B\sqrt{U}\right)\frac{1}{I_w^2}, \tag{1}$$

where A and B are the King's law coefficients, and I_w is the wire current. The previous formula shows that by operating a hot-wire at extremely low currents or overheat ratios, it is possible to transform it into a Cold-Wire (CW). Cold-wires are rarely operated in Constant Temperature Anemometry (CTA) mode given the highly nonlinear response exhibited by the bridge's feedback loop at low overheat ratios [29]. Furthermore, operating a CW in CCA mode has the additional advantage that the output voltage scales linearly with temperature, significantly simplifying the calibration procedure [30]: $E = A_c + B_c T_a$.

During the experiments, two Dantec Dynamics 55P15 boundary layer probes are placed at 6 mm distance and forming a 45° angle (see Fig. 1) to enable quasi-simultaneous velocity and temperature readings. During the post-processing, the spatial lag is accounted to correct the HWA calibration with the CW temperature at the corresponding point.

It should be noted that the aspect ratio of the cold-wire probe, AR = l_w/d_w = 1.25/0.005 = 250, can significantly limit the frequency response of the thermal measurements. Nevertheless, this does not represent a concern in these experiments since only the mean temperature is of interest to correct the HWA calibration. Additionally, thanks to the stationary nature of the CF vortices studied herein, their footprint on the thermal field will be captured by the CW signal.

The HW probe is connected to a TSI IFA-300 constant temperature bridge, while the CW probe is connected to a DISA 55M01 main unit equipped with a 55M20 constant current bridge module. The probes are translated in X, Y and Z directions using an automated three degrees-of-freedom traversing system placed downstream of the STEP model (see Fig. 1), with a positional accuracy of ± 6.2 μm. Additionally, the sting supporting the dual-probe features an embedded accelerometer[††] to register its vibrational motion in X, Y and Z directions. This is important to separate the natural resonance frequencies of the supporting structure from the flow-related spectral content recorded by the HWA.

Seven yz planes (i.e. parallel to the LE and normal to the surface) are scanned with HWA and CWA at different x stations in adiabatic and wall-heating conditions to capture the spanwise organization and streamwise growth of the crossflow vortices. Furthermore, measurements along an xz plane, within the range of $0.84 \le x/c_x \le 0.95$, are conducted at a fixed wall-normal location, $y/\delta_0^* = 3.70$. These measurements are intended to provide insights into

---

[††]Analogue Devices ADXL335.

6

Planes ID	P1	P2	P3	P4	P5	P6	P7	P_{xz}
x/c_x	0.29	0.40	0.51	0.62	0.73	0.84	0.95	$0.84 \leq x/c_x \leq 0.95$

Table 3   Streamwise stations of the different HWA/CWA planes, where P1 to P7 denote yz planes.

the transition front location. The selection of the wall-normal location for the xz plane is chosen to coincide with the maxima of the type I and type III secondary instability. The streamwise location of the HWA planes is indicated in Table 3.

Each yz plane, as well as the xz plane, successfully capture three periods (i.e. spatial wavelengths) of the primary stationary forced CF mode ($\lambda_z = 10$ mm). The yz planes are discretized into 54 uniformly distributed points in z direction and 41 sinusoidally spaced points in y direction (i.e. minimum Δy at the maxima of the stationary CFI). This discretization results in a resolution of $\Delta z = 555$ μm along z. The streamwise spacing between consecutive xz planes is set to $\Delta x/c_x = 0.108$, except for the final two planes (P6-P7), where $\Delta x/c_x = 0.114$ was used to effectively cover the region of laminar breakdown.

Both HWA and CWA measurements are acquired at a sampling rate of $f_s = 51.2$ kHz, resulting in a total measurement time of 2 seconds per point. The cut-off frequency of the HWA bridge is determined by means of a square-signal test which yields a cut-off frequency of 17 kHz.

HWA and CWA planes are measured by placing the probe in the freestream and gradually approaching the wall until the measured velocity is 10% of the external velocity, U_e. The distance from the last HWA/CWA point to the wall is determined using a Taylor-Hobson microalignment telescope, featuring a resolution of 20 μm. During the post-processing, a second strategy is used to enhance the precision of the wall distance measurement. This approach, detailed in Saric et al. [31], employs a linear regression to fit the last near-wall boundary layer points and estimate the wall $y-$coordinate. However, in the last two planes (P6 and P7), where the meanflow was significantly modulated by the highly amplified stationary CFI, only the optical wall measurement approach is used instead to establish the distance to the wall. Lastly, it is important to highlight that adiabatic and non-adiabatic planes were sequentially measured at identical streamwise locations.

C. Numerical framework

Compressible boundary layer solver

In the present work, baseflow and stability results obtained from in-house numerical solvers are presented to complement experimental results and improve the problem understanding. The numerical methodology is divided in two parts. First, the Compressible Boundary Layer (CBL) equations are solved to obtain the time-invariant and spanwise-invariant baseflow at a particular wall temperature distribution and freestream conditions. Secondly, the resulting perturbation solution from this baseflow is obtained using Compressible Linear Stability Theory (CLST).

The CBL equations for steady ($\partial/\partial t = 0$), plane boundary layer flows are solved. The boundary layer is three-dimensional but spanwise invariant ($\partial/\partial z = 0$ but $w = cst.$). The final set of equations can be written as follows [32]:

$$\frac{\partial \rho u}{\partial x} + \frac{\partial \rho v}{\partial y} = 0, \tag{2}$$

$$\rho \left(u \frac{\partial u}{\partial x} + v \frac{\partial u}{\partial y} \right) = \rho_e u_e \frac{\partial u_e}{\partial x} + \frac{\partial}{\partial y} \left(\mu \frac{\partial u}{\partial y} \right), \tag{3}$$

$$\rho \left(u \frac{\partial w}{\partial x} + v \frac{\partial w}{\partial y} \right) = \frac{\partial}{\partial y} \left(\mu \frac{\partial w}{\partial y} \right), \tag{4}$$

$$\rho c_p \left(u \frac{\partial T}{\partial x} + v \frac{\partial T}{\partial y} \right) = -u \rho_e u_e \frac{\partial u_e}{\partial x} + \frac{\partial}{\partial y} \left(k \frac{\partial T}{\partial y} \right) + \mu \left(\frac{\partial u}{\partial y} \right)^2 + \mu \left(\frac{\partial w}{\partial y} \right)^2, \tag{5}$$

$$p = \rho R T, \tag{6}$$

where the subscript $_e$ denotes edge parameters. Note that there are effectively 5 unknowns (u, v, w, ρ, T) since the remaining parameters (μ and k) can be expressed as a function of temperature via Sutherland's law. At the wall, the

7

no-slip ($u = 0$ and $w = 0$) and no-penetration ($v = 0$) conditions are specified together with the wall temperature (T_w) or the heat flux ($\partial T / \partial y|_w = 0$). In non-adiabatic conditions, the wall temperature distribution is retrieved from COMSOL simulations reproducing the experimental conditions, see Fig. 2.

The edge parameters are retrieved from the external velocity distribution derived from the experimental C_p (see Fig. 2). To ensure smoothness in the numerical solution, the external velocity distribution is expressed in terms of a polynomial fit of logarithmic basis:

$$U_e / U_0 = 0.0085 \ln (x + x_0)^5 + 0.0894 \ln (x + x_0)^4 + 0.3728 \ln (x + x_0)^3 + 0.7926 \ln (x + x_0)^2 ...$$
$$+ 0.9878 \ln (x + x_0) + 1.6830,$$

with $x_0 = 0.01$ m. Following the formulation presented in Liu [32], a Compressible Falkner-Skan Cooke (C-FSC) profile is set at the inflow ($x/c_x = 0.06$) given the Hartree parameter ($\beta_H = 0.4$) and the wall temperature or the heat flux. Eq. 2–5 are solved in a grid featuring a uniform spacing in x-direction ($n_x = 1000$) and pseudo-spectral discretization in wall-normal direction by means of $n_y = 200$ Chebyshev polynomials. The collocation points in the y-direction are clustered near the wall to ensure that regions where strong gradients occur are properly resolved. The derivatives are approximated using a second-order backward Euler (implicit) scheme in streamwise direction and pseudo-spectral Chebyshev differentiation matrices in wall-normal direction.

The remaining parameters necessary to initialize the CBL simulation are:

$$\text{Pr} = 0.71, \quad \gamma = 1.4, \quad R = 287 \text{ J/kgK} \quad U_0 = U_\infty \cos \Lambda = 11.07 \text{ m/s},$$
$$\delta_0 = 5.80 \times 10^{-4} \text{ m}, \quad T_0 = 299.18 \text{ K}, \quad \text{and} \quad \rho_0 = 1.18 \text{ kg/m}^3;$$

where $\Lambda = 45°$ and δ_0 is the Blasius length scale, defined using as reference length $x = 0.4c_x$.

Compressible linear stability solver

The compressible linear stability equations are obtained by distinguishing between a steady laminar solution (i.e. baseflow, $\bar{q}$) and small perturbations on the velocity components, the density and the temperature (i.e. disturbances, $q' = [u', v', w', \rho', T']$):

$$q = \bar{q} + q'. \tag{7}$$

Introducing this decomposition into Equations 1–5, subtracting the mean-flow terms, neglecting the quadratic disturbance terms (i.e. non-linear terms), assuming parallel flow ($\partial \bar{q}/\partial x = 0$ and $\bar{v} = 0$), and defining the disturbances as wave-like solutions ($q' = \hat{q}(y)e^{i(\alpha x + \beta z - \omega t)}$), the final set of equations comprising the CLST solver can be obtained [15, 33]. For spatially-evolving problems, these equations constitute a non-linear eigenvalue problem in α which can be solved independently at every x station (local) given the proper boundary conditions. At the wall, no-slip conditions are imposed for the disturbances:

$$\hat{u}(0) = 0, \quad \hat{v}(0) = 0, \quad \hat{w}(0) = 0. \tag{8}$$

If the disturbance features a high-frequency, the wall cannot modify the temperature of the perturbation and therefore $\hat{T}(0) = 0$ holds. Conversely, given the stationary nature of crossflow vortices, the wall can modify the temperature of the stationary CFI. Therefore, this boundary condition must be changed to $\partial \hat{T}/\partial y(0) = 0$, so that a zero net-flux from the surface to the disturbance is instead established when simulating stationary CFI [33].

At the far-field, the top boundary condition reads ($y \to \infty$):

$$\hat{u}(y) = 0, \quad \hat{v}(y) = 0, \quad \hat{w}(y) = 0, \quad \hat{p}(y) = 0, \quad \text{and} \quad \hat{T}(y) = 0. \tag{9}$$

In what follows, disturbances are assumed to grow in space, in line with the observed spatial nature of convective instabilities developing in boundary layers. Therefore, their frequency is real (ω_r) but their wavenumbers are complex in streamwise ($\alpha = \alpha_r + \alpha_i$) and spanwise ($\beta = \beta_r + \beta_i$) direction. The disturbance concerned in this work is the stationary CFI, which features $\omega = 0$ and, due to the spanwise invariant condition of the baseflow, it experiences growth only in streamwise direction (i.e. $\beta = \beta_r$ and $\alpha = \alpha_r + \alpha_i$).

Analogous to the discretization scheme employed in the CBL solver, a spectral collocation method based on Chebyshev polynomials as basis functions is used to approximate the differentiation matrices constituting the eigenvalue problem.

The system of equations comprising the non-linear eigenvalue problem can be subdivided in three different terms multiplying the eigenvalue (α) and eigenfunctions ($\phi = [\hat{u}, \hat{v}, \hat{w}, \hat{p}, \hat{T}]$) as $A\phi = \alpha B\phi + \alpha^2 C\phi$. The companion matrix

8

method [34] is employed to express the previous system as a generalized eigenvalue problem ($Av = \lambda Bv$) and solve for α.

Once the eigenvalue (α) and eigenfunctions (ϕ) are known, it remains to identify which eigensolutions are physical. To do so, an ad-hoc filter, herein denoted as eigenvalue filter, selects those eigenfunctions that follow more closely an exponential decay in y of the form [35]:

$$\phi = \exp\left(-i\left(\sqrt{\alpha_r^2 + \beta_r^2}\right)y\right).$$

D. Flow metrics and non-dimensional parameters

This subsection introduces the non-dimensional parameters and criteria used throughout Sec. III to present both experimental and numerical results. Additionally, the metrics employed to characterize the features associated with the time-averaged flow, the primary and secondary CFI are also introduced.

The experimental and numerical results presented herein have been normalized differently in x, y, and z directions. The non-dimensionalization of the x-coordinate is based on the model chord, i.e. $c_x = 0.6$ m. For the non-dimensionalization of the y-coordinate, the displacement thickness in adiabatic conditions from CBL results at $x/c_x = 0.29$, i.e. $\delta_0^* = 0.603$ mm, is used. Finally, the spanwise coordinate (z) is non-dimensionalized with the primary stationary CFI wavelength, $\lambda_z = 10$ mm.

In the following section, velocity results from the numerical simulations are presented alongside HWA measurements. To guarantee a meaningful comparison between the two, numerical results will be expressed in terms of the resulting velocity component read at the hot-wire, Q, defined as [36]:

$$Q = \sqrt{(u\cos\Lambda + w\sin\Lambda)^2 + v^2}. \tag{10}$$

To ensure consistency between this definition and the experimental measurements, the traversing system is carefully aligned with the model's global coordinate system (X, Y, Z) during the experiments. This alignment ensures that the velocity components read by the wire correspond to the projections of u and w onto the global X coordinate, and v onto the Y coordinate, as indicated in [37] (see HWA sketch in Fig. 1).

The stationary CFI ($\langle q'\rangle_z$) is retrieved from the spanwise root-mean-square of the time-averaged flow ($\overline{Q}$). This methodology has been previously outlined and effectively employed in prior studies investigating the stability of CFI (e.g. [27, 37, 38]). In this work, the amplitude of the stationary CFI is defined as the wall-normal integral of the spanwise root-mean-square:

$$\langle q'\rangle_z = \text{RMS}\left(\overline{Q} - \langle\overline{Q}\rangle_z\right), \tag{11}$$

$$A = \frac{1}{y_m}\int_0^{y_m}\langle q'\rangle_z\mathrm{d}y, \tag{12}$$

where $\langle\overline{Q}\rangle_z$ denotes the spanwise averaged meanflow and y_m is the maximum wall-normal coordinate.

For the study of the unsteady perturbation field, the Power Spectral Density (PSD) function of the time-dependent velocity signal is analyzed. From the PSD data, the different frequency bands associated with the relevant secondary instabilities can be identified. Then, the fluctuating signal from the HWA planes is bandpassed at the identified frequency bands using an 8th order Butterworth filter. The root-mean-square (RMS) signal of each frequency band serves as an indicator of the development of the primary travelling CFI (i.e. low frequency) and secondary CFI (i.e. high frequency). To effectively quantify their amplitude and growth, the RMS of the bandpassed signal is integrated along the yz planes, following the approach outlined in other related studies (e.g. [38, 39]):

$$a_{\text{rms}} = \frac{1}{y_m}\frac{1}{z_m}\int_0^{y_m}\int_0^{z_m}\sigma_{Q,\text{BP}}\mathrm{d}z\mathrm{d}y. \tag{13}$$

Finally, the power spectra of the velocity fluctuations is also used throughout the analysis of the unsteady perturbation content. Welch's Modified Periodogram method (i.e. Welch's method) is used herein to compute the PSD and reduce the noise of the signal. The signal is subdivided in segments of 10 samples length overlapped by 50 %. A Bartlett window is applied to each segment to minimize spectral leakage. The subsequent window overlapping mitigates the loss of information at the segment margins produced by the Bartlett window. Each signal segment is Fourier transformed and later squared to compute the corresponding periodogram. Lastly, the periodograms are averaged to reduce the variance of the power spectrum.

9

III. Results in adiabatic and wall-heating conditions

This section presents the experimental and numerical results concerning the development of a boundary layer on a swept flat plate subject to adiabatic and wall-heating conditions. Initially, the influence of a non-adiabatic wall condition on the time-averaged flow will be discussed based on the experimental and CBL simulations. Subsequently, the impact of a non-adiabatic wall on the stability of the boundary layer will be analyzed by examining the change in growth of the stationary crossflow instability (stationary CFI) from experimental and numerical results. Finally, the impact of wall-heating on the development of secondary instabilities and subsequent laminar breakdown will be discussed.

A. Impact on the time-averaged flow

Fig. 3 presents the boundary layer integral parameters under adiabatic and wall-heating conditions, derived from both experimental and CBL results. Good agreement between experimental and numerical results is evident until approximately $x/c_x \approx 0.62$. However, beyond this point, a departure between experimental and numerical results occurs due to the substantial distortion induced by the strongly amplified CF vortices on the meanflow. The imparted distortion on the meanflow is clearly reflected in the velocity profiles depicted in Fig. 4a, derived from the spanwise averaging of the velocity fields presented in Fig. 5. The strong amplification of stationary CFI leads to significant nonlinear interactions between the primary CFI and its harmonics, especially in the last yz planes. The amplification of the primary CFI and its harmonics contributes to the loss of spanwise periodicity on the time-averaged velocity field, resulting in the strong modulation evident from the spanwise-averaged velocity profiles at $x/c_x = [0.73, 0.84, 0.95]$ in Fig. 4a.

Similar conclusions can be inferred from the temperature profiles depicted in Fig. 4b, resulting from spanwise-averaging the mean temperature fields shown in Fig. 6. Initially, the velocity profiles obtained from experiments align well with CBL results up to $x/c_x \approx 0.62$. However, beyond this point, the temperature profile exhibits a significant modulation due to the substantial redistribution of temperature along the z-coordinate, correlating with areas of high and low momentum in the velocity fields. This correlation becomes evident when comparing the velocity fields presented in Fig. 5 with the temperature fields in Fig. 6.

Both numerical and experimental results show an increase in momentum deficit within the boundary layer with wall-heating, as observed from Fig. 3. This phenomena can be better illustrated by analyzing the boundary layer equations at the wall [20]:

$$\left.\frac{\partial^2 u}{\partial y^2}\right|_{y=0} = \frac{\mathrm{Re}}{\mu}\frac{dp_e}{dx} - \frac{1}{\mu}\frac{\partial \mu}{\partial y}\frac{\partial u}{\partial y}\bigg|_{y=0}, \tag{14a}$$

$$\left.\frac{\partial^2 w}{\partial y^2}\right|_{y=0} = -\frac{1}{\mu}\frac{\partial \mu}{\partial y}\frac{\partial w}{\partial y}\bigg|_{y=0}. \tag{14b}$$

The flow case concerned herein is subject to a favorable pressure gradient, $dp_e/dx < 0$, which then yields an always negative $\partial^2 u/\partial y^2$, i.e. no flow reversal. Wall-heating results into a negative $\partial \mu/\partial y$ at the wall, rendering the term
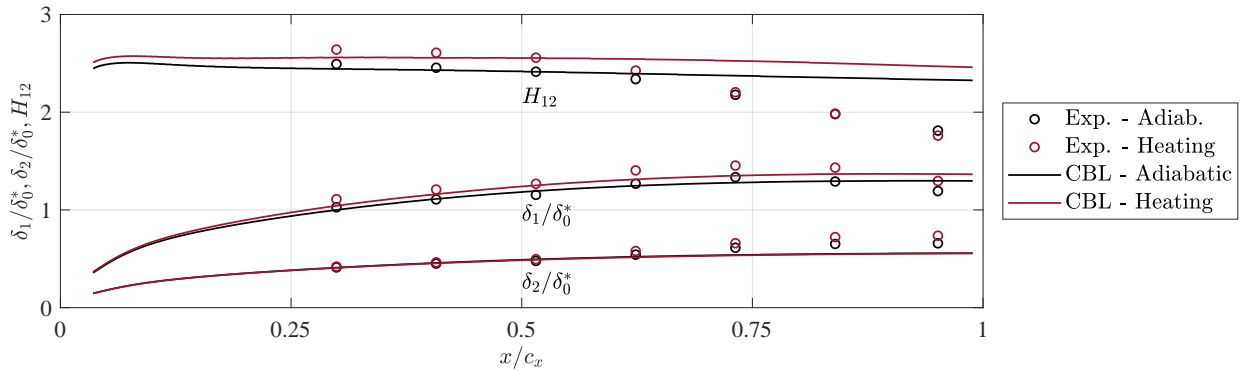

Fig. 3   Integral parameters from CBL solution (solid lines) and experimental results (symbols) in adiabatic and wall-heating conditions.
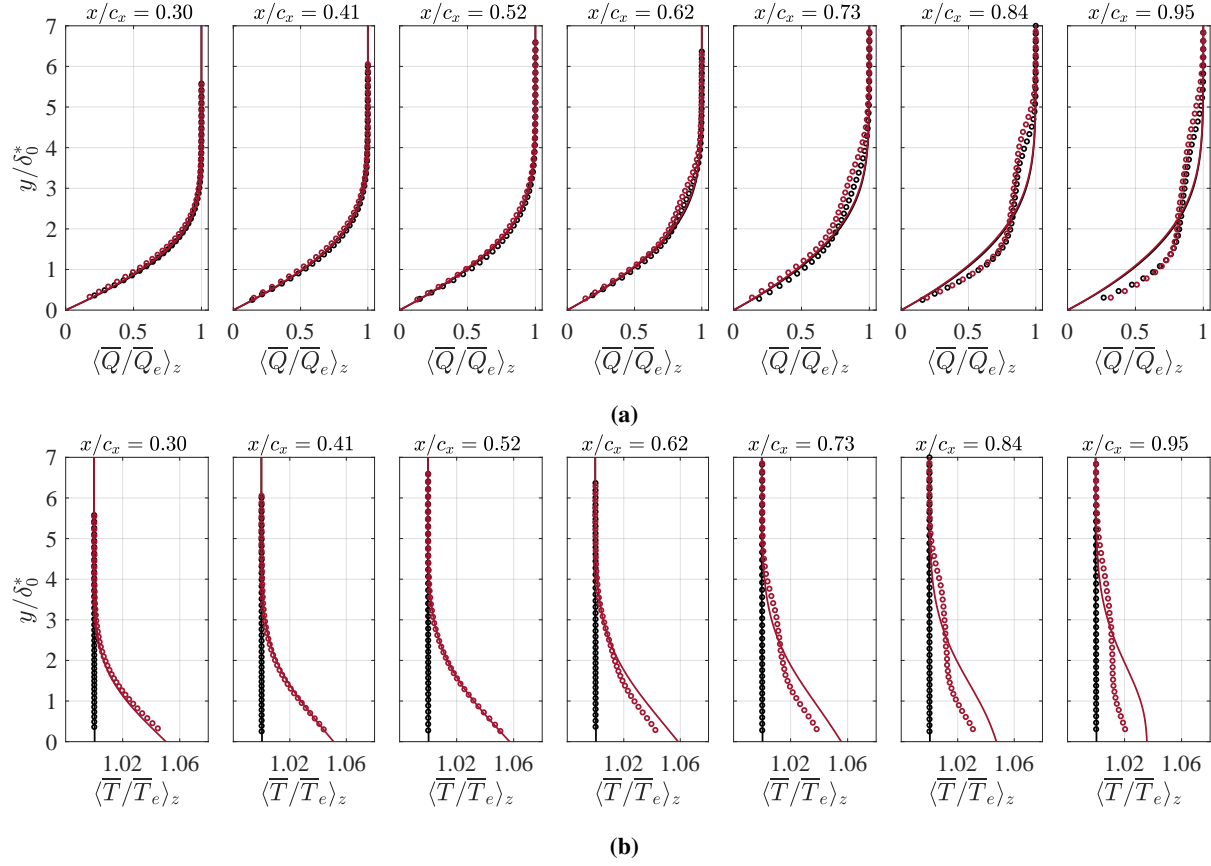
Fig. 4 **Boundary layer profiles from experimental (symbols) and CBL (lines) results under adiabatic (black) and wall-heating (red) conditions. (a) Velocity profiles and (b) temperature profiles at different streamwise locations.**

$\partial^2 u/\partial y^2$ less negative (see Eq. 14a), and resulting into a velocity profile which exhibits more momentum deficit, in line with results presented in Fig. 3. The net effect of increasing the momentum deficit within the boundary layer results in a movement of the crossflow inflection point away from the wall, increasing the inviscid instability derived from the crossflow component, the stationary CFI, thus further destabilizing the flow [15]. The following section will dive into the destabilizing effect of wall-heating on the stationary CFI.

B. Impact on the steady perturbation

As discussed in Sec. III.A, the presence of an inflection point within the crossflow component (w_s) is a fertile condition for an inviscid instability, which manifests in the velocity field as a series of co-rotating vortices. The spatial organization and streamwise evolution of the crossflow vortices under both adiabatic and wall-heating conditions, as retrieved from the HWA yz planes, are presented in Fig. 5. Initially, the disturbance displays low amplitude and exhibits strong periodicity in the spanwise direction. However, as the instability grows in streamwise direction, the stationary CFI attains significant amplitude, notably distorting the meanflow and triggering non-linear interactions between the primary CFI and its harmonics. This interaction contributes to the loss in periodicity observed in the final HWA planes, as shown in Fig. 5.

The spatial organization of the temperature field, as retrieved from the CWA yz planes under wall-heating conditions, is presented in Fig. 6. These results portray the redistribution of temperature along yz planes induced by the action of the in-plane velocity components, w and v. Both spanwise (w) and wall-normal (v) velocity components are driven by the action of the crossflow vortices, resulting in a high spatial correlation between the temperature and the velocity fields, as portrayed in Fig. 5.

Differences in the steady perturbation field between adiabatic and wall-heating conditions are particularly apparent from the last HWA measurement planes, as shown in Fig. 5. In particular, examination of the last HWA plane at
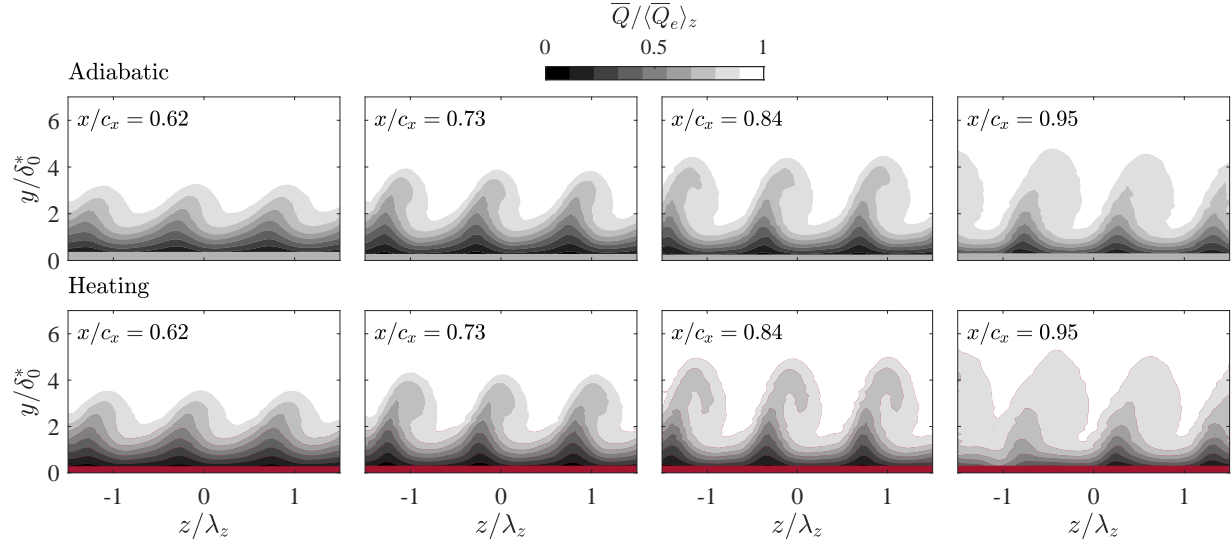
11

Fig. 5   Contours of the time-averaged velocity field at different yz planes from HWA measurements in adiabatic (gray wall) and wall-heating (red wall) conditions. Positive z corresponds to the outboard side of the model, with $z = 0$ indicating the model's centerline.
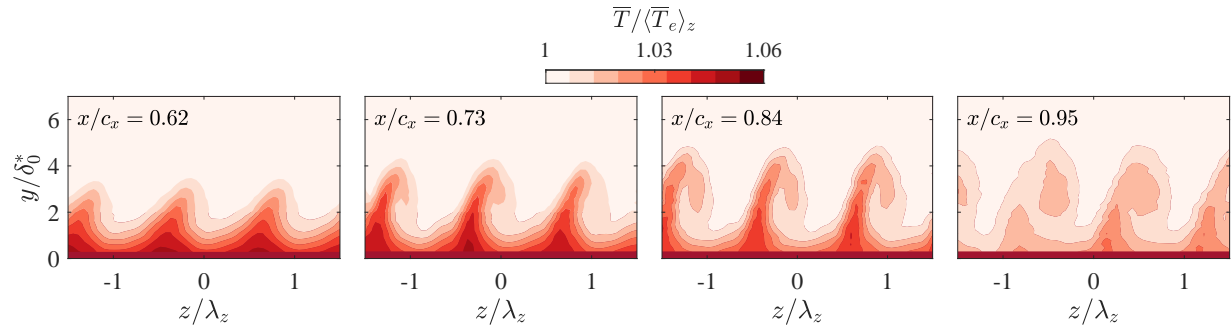

Fig. 6   Contours of the time-averaged temperature field at different yz planes from CWA measurements in wall-heating conditions.

$x/c = 0.95$ reveals an earlier onset of flow breakdown under wall-heating conditions compared to adiabatic conditions. The enhanced destabilization undergone by the perturbation field with wall-heating becomes more evident upon analyzing the steady disturbance profiles presented in Fig. 7, calculated as indicated in Eq. 11.

At the initial streamwise stations ($x/c_x \leq 0.62$), the steady disturbance profiles ($\langle q' \rangle_z$) shown in Fig. 7 display a unique maximum or lobe along y, a common feature of stationary CFI in the linear regime. However, at the last streamwise stations, a secondary lobe emerges above the primary one within the steady disturbance profile. This is a well-established feature of CF vortices that has been previously ascribed to the emergence of non-linear interactions among the primary mode and its harmonics (e.g.[38, 40, 41]). This secondary lobe manifests as a consequence of the roll-over of the crossflow vortices [40], particularly noticeable in the last yz planes of Fig. 5 (i.e. $x/c_x = [0.73, 0.84, 0.95]$).

The relevance of non-linear interactions along the streamwise direction is shown in Fig. 8, where the amplitude evolution of the fundamental CF mode together with the second and third harmonics is shown. The different harmonics are calculated conducting a spanwise FFT at every y station on the steady perturbation signal (q'), as illustrated in Fig. 8. The amplitude (A) presented in Fig. 8c results from integrating the steady perturbation profile for each mode, $\langle q_{m(0,n)} \rangle_z$, along the wall-normal direction, following the methodology outlined in [38] and specified in Eq. 12. This metric is particularly convenient to reliably compare adiabatic and non-adiabatic results in the non-linear regime, where most of the amplification stems from the stronger wall-normal modulation of the perturbation profile. In agreement with previous studies (e.g. [40]), it is noted that under both wall-heating and adiabatic conditions, the emergence of a second
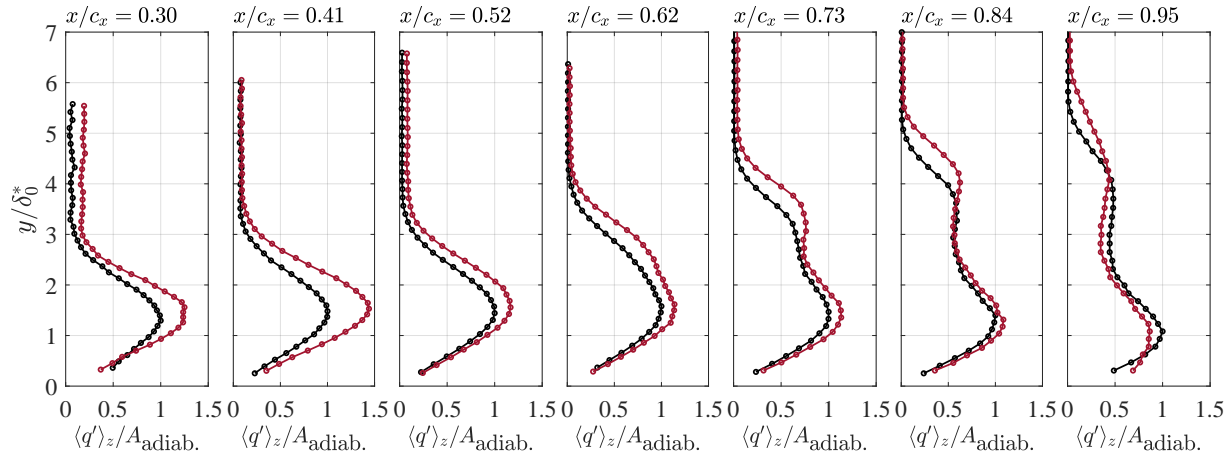
12

Fig. 7   Steady perturbation profile ($\langle q' \rangle_z$) at different streamwise stations from experimental results in adiabatic (black) and wall-heating (red) conditions.
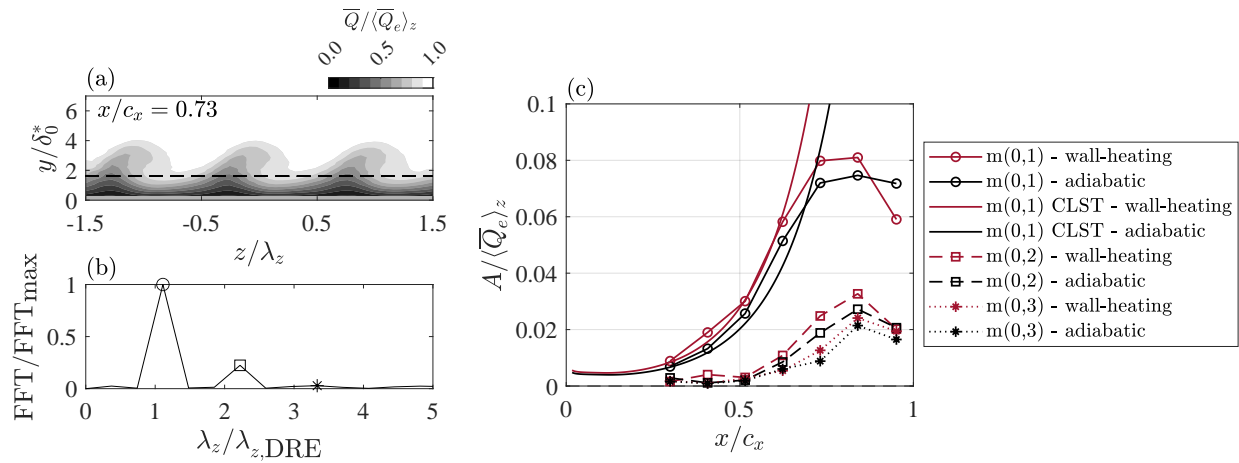

Fig. 8   (a) Contours of the time-averaged velocity field for Plane 5, $x/c_x = 0.73$, and corresponding (b) spectral decomposition resulting from performing a spanwise FFT at the y station indicated by a dashed line in (a). (c) Amplification of the primary stationary CFI mode, 2nd and, 3rd harmonics in adiabatic (black) and wall-heating (red) conditions.

lobe on the steady perturbation profile, as shown in Fig. 7, coincides with the saturation of the primary CF mode (note $x/c = 0.73$ for wall-heating and $x/c = 0.84$ for adiabatic conditions). Concurrently, the observed saturation correlates well with the larger amplitude attained by the higher harmonics, as observed from the last x stations in Fig. 8c.

The experimental results presented in Figures 7 and 8 evince the destabilizing effect of wall-heating on the steady perturbation field. Notably, from Fig. 7, it can be inferred that most of the amplification on the steady perturbation takes place in the linear regime. In turn, the greater amplification experienced upstream is translated into an earlier saturation of the primary CFI with wall-heating. This is further confirmed with the results presented in Fig. 8, where the higher harmonics exhibit larger amplitude under wall-heating compared to adiabatic conditions.

C. Impact on unsteady perturbations

The results presented in the preceding section evince the significant distortion imparted by the highly amplified stationary CF vortices on the meanflow. This distortion yields strong spanwise and wall-normal velocity gradients, creating a fertile flow condition for the development of secondary CFI [38].

Insight into the spatial distribution of the temporal velocity fluctuations provides valuable information on the nature
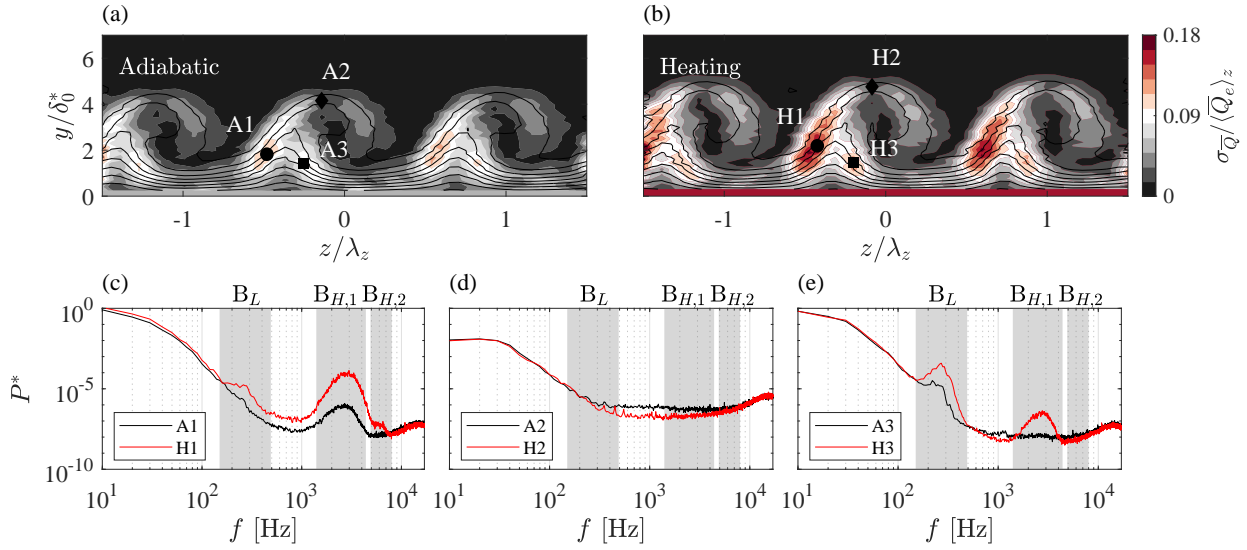
13

Plane 6, $x/c_x = 0.84$

Fig. 9 Contours of temporal velocity fluctuations and time-averaged velocity (black contour lines) in adiabatic (a) and wall-heating (b) conditions at yz plane P6, i.e. $x/c_x = 0.84$. Spectral distribution at probes A1 and H1 (c), A2 and H2 (d), and A3 and H3 (e). The location of the points where the spectral data has been extracted are indicated in (a) and (b).

and location of the secondary instabilities. Fig. 9a-b reveal significantly higher velocity fluctuations in wall-heating conditions than in adiabatic conditions. Remarkably, under wall-heating conditions, the magnitude of the velocity fluctuations at their maxima is two orders of magnitude higher than in adiabatic conditions. This observation is in agreement with the results presented in Sec. III.B, where the existence of a more amplified stationary CFI yields a stronger meanflow distortion and a premature development of secondary instabilities under wall-heating conditions.

The spectral distribution of the velocity fluctuations are particularly important to distinguish the different secondary instabilities emerging within the distorted velocity field. Fig. 9c-e show the Power Spectral Density (PSD) obtained at the upwelling region and inner side of the CF vortex, note the probes indicated in Fig. 9a-b. The PSD results are normalized as

$$P^* = \sqrt{(\Delta f P)/U_0^2} \tag{15}$$

following the criteria introduced in [25].

The spectral content presented in Fig. 9c-e exhibit two distinguished frequency bands of high velocity fluctuations centered around $f = 300$ Hz and $f = 3$ kHz, hereafter referred as B_L and B_H, respectively. The frequency range where these instabilities develop is in agreement with previous studies analyzing the unsteady development of crossflow instabilities [38]. The emergence of the instability at $f = 300$ Hz, known as type III [42], has been linked to the interaction between traveling and stationary crossflow instabilities [27, 38, 41]. On the other hand, the instability centered at $f = 3$ kHz, identified as type I, is an inviscid, Kelvin-Helmholtz instability [43] resulting from the large spanwise velocity gradients caused by the strong meanflow distortion. Notably, an additional peak adjacent to the $f = 3$ kHz bump emerges at $f \approx 6$ kHz, corresponding to the type-II secondary instability, previously observed within a similar frequency range in other studies (e.g. [37, 38]).

Previous works have associated the onset of the type-II secondary instability with the peak values of the wall-normal velocity gradients occurring near the upper region of the CF vortices, close to probe locations A2 and H2 as depicted in Fig. 9a-b. However, inspection of the velocity spectra at those locations exhibits very low velocity fluctuations. This observation aligns with the findings from Rius-Vidales et al. [22], where similar investigations into CF vortices development using an identical experimental framework (i.e. STEP) were conducted. Bandpassed velocity fluctuations within $B_{H,1}$ ($1.4 \leq f \leq 4.4$ kHz) and $B_{H,2}$ ($4.9 \leq f \leq 8$ kHz) render very low amplitude of the type-II secondary instability and a spatial proximity to the type-I mode, see Fig. 10. The latter suggests that the contribution of the type-II instability to the breakdown process is likely marginal compared to the type-I mode. Thus, for simplicity, subsequent
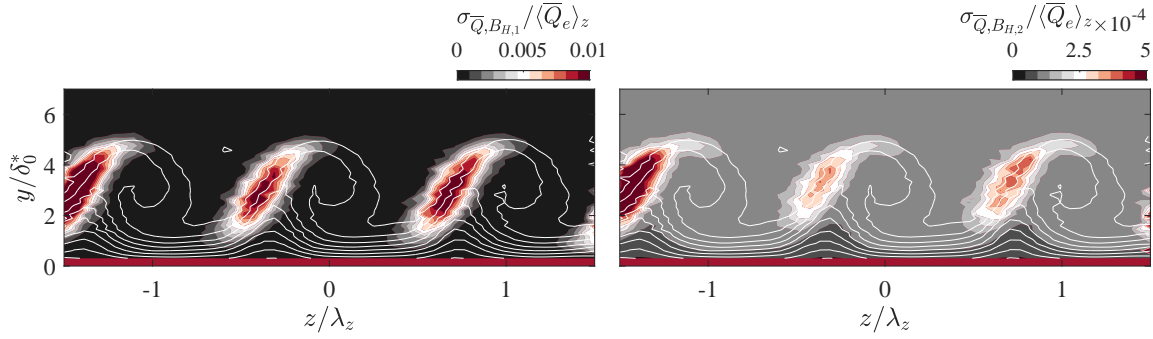
14

Fig. 10 Contours of temporal velocity fluctuations bandpassed at the frequency bands $B_{H,1}$ (left) and $B_{H,2}$ (right), indicated in Fig. 9c-e, under wall-heating conditions at Plane 6, i.e. $x/c_x = 0.84$. White contour lines delineate the time-averaged velocity field.
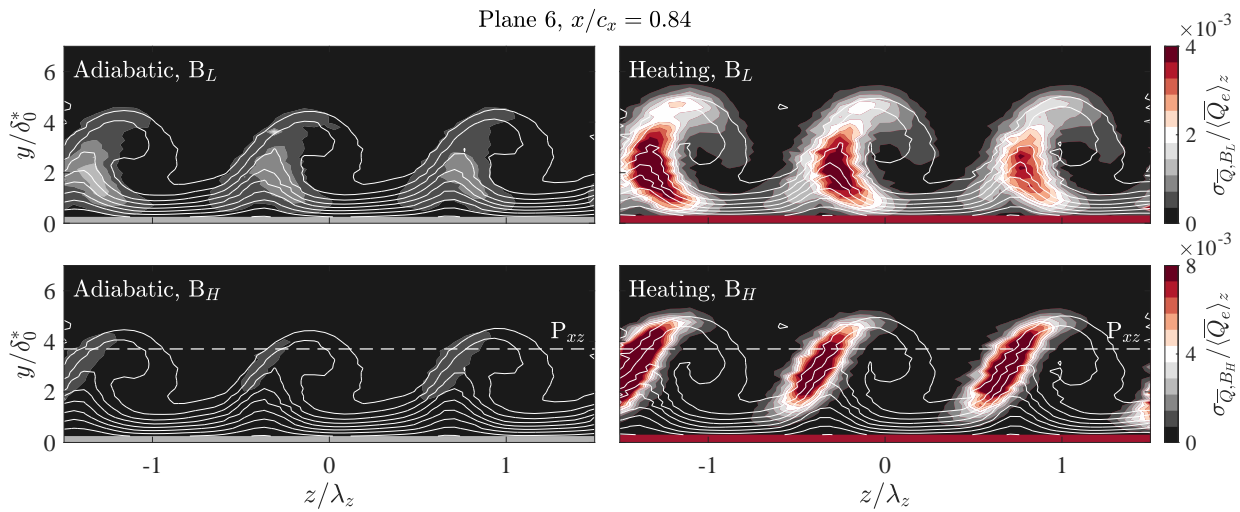

Fig. 11 Contours of temporal velocity fluctuations bandpassed at the frequency bands B_L and B_H, indicated in Fig. 9c-e. White contour lines delineate the time-averaged velocity field. A dashed white line indicates the wall-normal location where the xz plane is measured.

results presented herein encompass type-I and type-II instabilities within the same frequency band, denoted as B_H ($1.4 \leq f \leq 8$ kHz), while the type-III instability is represented within the frequency band B_L.

Fig. 11 portrays the spatial distribution of bandpassed velocity fluctuations within B_L ($150 \leq f \leq 490$ Hz) and B_H ($1.4 \leq f \leq 8$ kHz) frequency ranges under both wall-heating and adiabatic conditions. In agreement with previous studies (e.g. [27, 38]), the low-frequency fluctuations, ascribed to the type-III instability, exhibit higher intensity near the wall, on the inner side of the crossflow vortices, coinciding with the maxima of the spanwise velocity gradient. Conversely, high-frequency fluctuations, associated in this case mainly with the type-I secondary instability, attain high amplitudes at the low-momentum upwelling region, correlating with regions of minimum spanwise velocity gradient.

Higher amplitude disturbance levels are observed in wall-heating conditions for both low and high frequency fluctuations, as underlined by the contours presented in Fig. 11. To effectively evaluate the growth of the unsteady disturbances, the r.m.s. of the bandpassed signal is integrated along y and z in the HWA yz planes, as indicated in Eq. 13, following the methodology implemented in [39]. The results are presented in Fig. 12. In agreement with CLST results, the experimental data also exhibits higher amplification of the primary stationary CFI mode in wall-heating conditions within the linear regime. This premature amplification leads to an earlier saturation of stationary CFI in wall-heating conditions compared to the adiabatic case. Nonetheless, the saturation amplitude of the stationary CFI appears different from that in adiabatic conditions, where the stationary CF saturates at around $A_{\max}/\overline{Q}_e \approx 0.16$ (not shown here),
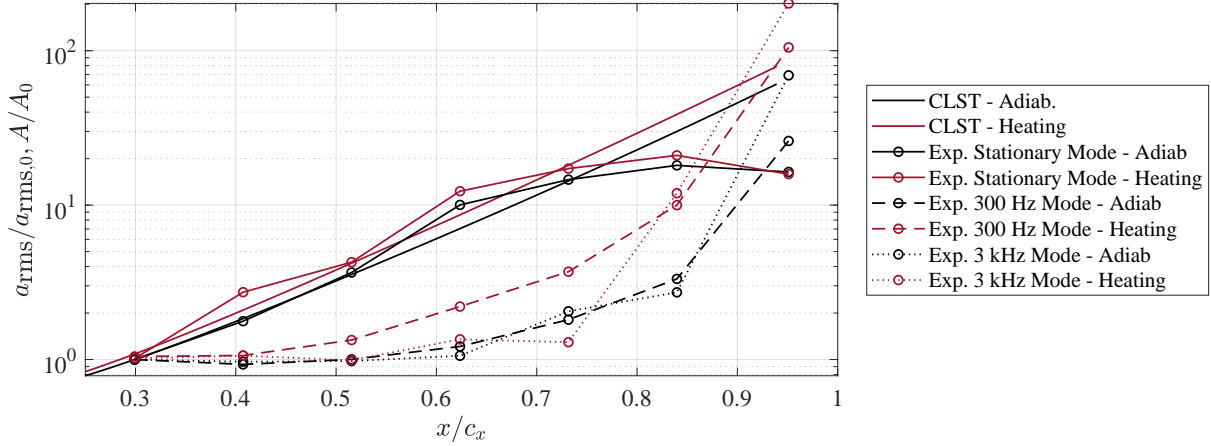
Fig. 12 Growth of the different unsteady modes in both wall-heating and adiabatic conditions. Experimental results are presented with symbols while numerical results are shown with solid lines. The data is normalized using the disturbance amplitude of each mode at the first x station in adiabatic conditions.

consistent with the amplitude at saturation reported in other experimental works with similar freestream turbulence intensity (e.g. see Fig. 19 in Downs and White [39]). The underlying cause of this behavior remains ambiguous, necessitating additional analysis. Further investigation on this is necessary to ascertain whether this observation stems from the effect of a heated wall on the perturbation field or from potential experimental errors.

The high-frequency (3 kHz mode) fluctuations, tied to the growth of type-I and type-II secondary instabilities, exhibit an explosive growth in the last streamwise stations (non-linear regime) preceding breakdown [38], as observed from Fig. 12. Under wall-heating conditions, the high-frequency fluctuations present considerably higher disturbance amplitude. The latter could be related to the stronger meanflow distortion imparted by the higher-amplitude stationary CFI caused with wall-heating. Conversely, the low-frequency disturbances (300 Hz mode) exhibit sustained growth along both linear and non-linear regime, decoupled from the saturation of the primary mode. These findings suggest that wall-heating significantly amplifies the underlying traveling CFI. Similar observations have been reported in the works of Eppink and Wlezien [17] and Ren and Kloker [15], where the authors' results present a strong stabilization of the travelling crossflow mode under cooled wall conditions and *viceversa*.

D. Effect on laminar flow breakdown

In order to quantify the onset to turbulence, the velocity fluctuations obtained from the xz HWA plane are bandpass filtered within a high-frequency band, spanning from $f = 12$ kHz to the HWA bridge cut-off frequency, $f = 17$ kHz. The aim is to isolate the increase of velocity fluctuations due to turbulent motion from those associated with the growth of secondary instabilities [37]. The wall-normal location of the P_{xz} is set in a region where the type-I secondary instability is prominent (note dashed line in Fig. 11). The results of the bandpass-filtered velocity fluctuations at P_{xz} are shown in Fig. 13. Furthermore, although not shown here, an additional xz plane was measured at a second wall-normal location covering the region where type-III secondary instabilities attain maximum amplitude. Results from the xz plane at the maxima of type-I instabilities exhibit earlier onset of laminar breakdown in streamwise direction than the xz plane acquired at the maxima of type-III instabilities, indicating that breakdown is driven by the type-I secondary instability.

Comparison between the high-frequency bandpass-filtered fluctuations in adiabatic and wall-heating conditions from Fig. 13 reveals a premature onset of turbulent wedges under wall-heating. By averaging the results from Fig. 13a-b in spanwise direction, the streamwise evolution of high-frequency velocity fluctuations is discerned. Assuming a similar spanwise organization of the transition front in both adiabatic and wall-heating conditions, an estimation of the advancement of turbulent breakdown under wall-heating is outlined in Fig. 13c, indicating an approximate value of $\Delta x/c = 6.48$ %. It is important to emphasize that this value does not correspond to the laminar-to-turbulent transition advancement typically derived from measurements acquired at the wall, such as those obtained through Infrared Thermography or Temperature Sensitive Paint. However, the observed advancement in the onset of flow breakdown offers plausible evidence that laminar-to-turbulent transition might undergo significant advancement in the
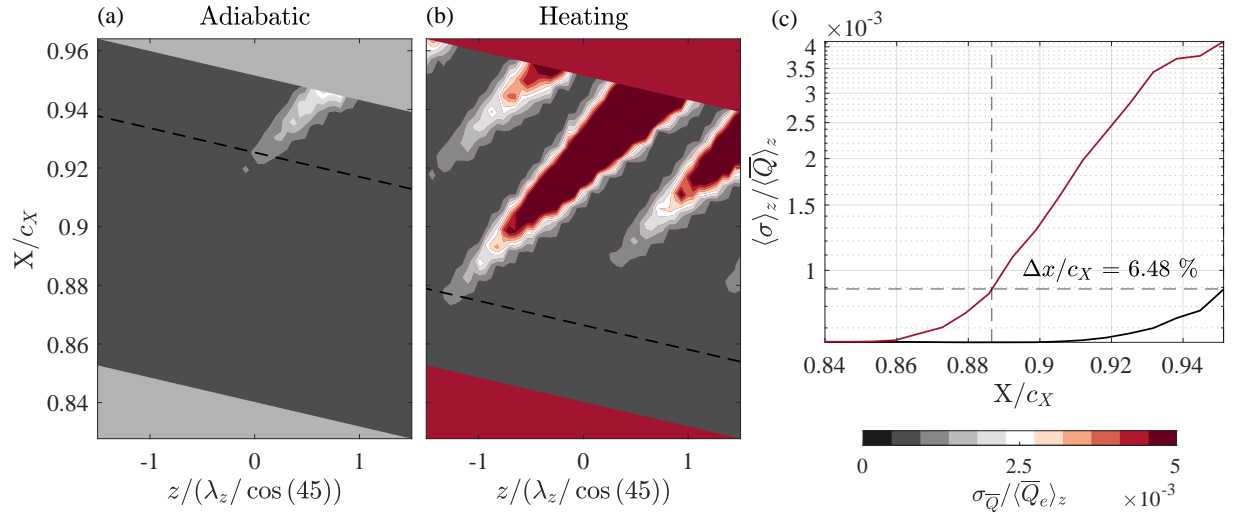
Fig. 13   Contours of the temporal velocity fluctuations bandpassed at $12 \leq f \leq 17$ kHz in adiabatic (a) and wall-heating (b) conditions. Results are obtained from HWA measurements conducted in a xz plane ($\mathbf{P}_{xz}$). (c) Streamwise growth of the spanwise-averaged bandpassed velocity fluctuations shown in (a) and (b).

presence of a heated wall.

IV. Conclusions

The present work investigates the impact of a heated wall on the development of crossflow vortices and subsequent laminar breakdown, using experimental methods and stability analysis.

Both experimental (i.e. HWA) and numerical (Compressible Boundary Layer solver) results exhibit a higher deficit in boundary-layer momentum due to wall-heating, in agreement with well-established boundary-layer theory. This notably affects the development of the stationary CFI, as the displacement of the inflection point upwards in wall-normal direction enhances the growth of the instability [15, 20]. This effect becomes evident when comparing yz HWA planes under adiabatic and wall-heating conditions, with the latter revealing a more pronounced meanflow modulation at identical streamwise locations. Examination of the spanwise-averaged steady perturbation profile, displaying higher amplitude under wall-heating conditions, confirms the destabilization undergone by the stationary CFI in the presence of a heated wall. Furthermore, the earlier onset of a second lobe on the steady perturbation profile under wall-heating conditions indicates the premature emergence of non-linear interactions. This observation is further corroborated by the higher-amplitude harmonics obtained under wall-heating conditions through a spanwise FFT analysis of the yz HWA planes.

The spectral analysis of the HWA signal reveals significantly higher velocity fluctuations under wall-heating compared to adiabatic conditions. In particular, peak velocity fluctuations increase by two orders of magnitude with wall-heating compared to adiabatic conditions. Under the investigated experimental conditions, most of the energy of the velocity fluctuations is encompassed under two different instabilities: a low-frequency instability at $f = 300$ Hz and a high-frequency instability at $f = 3$ kHz. Based on their frequency and the spatial organization of the bandpass-filtered signal, the low-frequency instability aligns with the type-III secondary mode, while the high-frequency instability corresponds to the type-I secondary instability. Both instabilities exhibit substantially higher amplitude in the presence of a heated wall, yet their growth behavior differs. While the type-I secondary instability exhibits premature explosive growth with wall-heating, the type-III secondary instability gradually amplifies in the streamwise direction, i.e. both in the liner and non-linear regime. Given the nature of the type-III instability, linked to the interaction between primary and traveling CFI, these findings suggest that the traveling CFI might be substantially amplified in the presence of a heated wall.

The global impact of wall-heating on the laminar breakdown has been investigated by examining the high-frequency content of the HWA signal along an xz plane. The results, obtained at a wall-normal position corresponding to the initiation of type-I instability breakdown, reveal an evident premature onset of turbulent motion in the presence

17

of a heated wall. Preliminary analysis suggests a transition advancement of approximately $\Delta x/c_x \approx 6.48\%$ under wall-heating conditions.

The aforementioned findings underscore the substantial influence of wall-heating on the stability and laminar breakdown of crossflow instabilities, notably evident even at relatively low temperature ratios, i.e. $T_w/T_\infty \approx 1.055$. Consequently, when assessing the effectiveness of technologies leveraging the dissipation potential of aerodynamic surfaces, like Outer Mold Line (OML) cooling, it becomes imperative to accurately quantify the effects of wall-heating on laminar-turbulent transition.

References

[1] Coutinho, M., Bento, D., Souza, A., Cruz, R., Afonso, F., Lau, F., Suleman, A., Barbosa, F. R., Gandolfi, R., Junior, W. A., et al., "A review on the recent developments in thermal management systems for hybrid-electric aircraft," *Applied Thermal Engineering*, 2023, p. 120427.

[2] Kellermann, H., Lüdemann, M., Pohl, M., and Hornung, M., "Design and optimization of ram air–based thermal management systems for hybrid-electric aircraft," *Aerospace*, Vol. 8, No. 1, 2020, p. 3.

[3] Ahluwalia, R., Wang, X., Kwon, J., Rousseau, A., Kalinoski, J., James, B., and Marcinkoski, J., "Performance and cost of automotive fuel cell systems with ultra-low platinum loadings," *Journal of Power Sources*, Vol. 196, No. 10, 2011, pp. 4619–4630. https://doi.org/https://doi.org/10.1016/j.jpowsour.2011.01.059, URL https://www.sciencedirect.com/science/article/pii/S0378775311001765.

[4] Kellermann, H., Habermann, A. L., and Hornung, M., "Assessment of aircraft surface heat exchanger potential," *Aerospace*, Vol. 7, No. 1, 2019, p. 1.

[5] Sozer, E., Maldonado, D., Bhamidipati, K., and Schnulo, S. L., "Computational evaluation of an oml-based heat exchanger concept for heather," *2020 AIAA/IEEE Electric Aircraft Technologies Symposium (EATS)*, IEEE, 2020, pp. 1–22.

[6] Habermann, A. L., Khot, A., Lampl, D. E., and Perren, C., "Aerodynamic Effects of a Wing Surface Heat Exchanger," *Aerospace*, Vol. 10, No. 5, 2023, p. 407.

[7] Kachanov, Y. S., Koslov, V. V., and Levchenko, V. Y., "Experimental Study of the Influence of Cooling on the Stability of Laminar Boundary Layers," *Izvestia Sibirskiogo Otdielenia Ak. Nauk SSSR, Seria Technicheskikh Nauk*, 1974, pp. 8–2.

[8] Costantini, M., Risius, S., and Klein, C., "Surface temperature effects on boundary-layer transition at various subsonic Mach numbers and streamwise pressure gradients," *New Results in Numerical and Experimental Fluid Mechanics XII: Contributions to the 21st STAB/DGLR Symposium, Darmstadt, Germany, 2018*, Springer, 2020, pp. 155–164.

[9] Boehman, L. I., and Mariscalco, M. C., "Stability of highly-cooled compressible laminar boundary layers," *Final Report*, 1976.

[10] Lekoudis, S. G., "Stability of the Boundary Layer on a Swept Wing with Wall Cooling Spyridon," *AIAA Journal*, Vol. 18, No. 9, 1980, pp. 1029–1035.

[11] Dovgal, A., Levchenko, V. Y., and Timopeev, V., "Boundary layer control by a local heating of the wall," *Laminar-Turbulent Transition: IUTAM Symposium Toulouse/France September 11–15, 1989*, Springer, 1990, pp. 113–121.

[12] Masad, J. A., "Transition in flow over heat-transfer strips," *Physics of Fluids*, Vol. 7, No. 9, 1995, pp. 2163–2174.

[13] Kral, L. D., Wlezien, R. W., Smith, J. M., and Masad, J. A., "Boundary-layer transition control by localized heating: DNS and experiment," *Transition, Turbulence and Combustion: Volume I Transition*, Springer, 1994, pp. 355–367.

[14] Mack, L. M., "On the stabilization of three-dimensional boundary layers by suction and cooling," *Symposium in laminar-turbulent transition*, edited by R. Eppler and H. Fasel, Springer, Stuttgart, Germany, 1980, pp. 223–238.

[15] Ren, J., and Kloker, M., "Instabilities in three-dimensional boundary-layer flows with a highly non-ideal fluid," *Journal of Fluid Mechanics*, Vol. 951, 2022, p. A9. https://doi.org/10.1017/jfm.2022.845.

[16] Bertolotti, F., and Bieler, H., "Stability Analysis of two-and three-dimensional Boundary Layer Flows with varied Wall Temperatures," *New Results in Numerical and Experimental Fluid Mechanics: Contributions to the 10th AG STAB/DGLR Symposium Braunschweig, Germany 1996*, Springer, 1997, pp. 64–70.

[17] Eppink, J., and Wlezien, R., "Data analysis for the NASA/Boeing hybrid laminar flow control crossflow experiment," *41st AIAA Fluid Dynamics Conference and Exhibit*, 2011, p. 3879.

[18] Lemarechal, J., Costantini, M., Klein, C., Kloker, M. J., Würz, W., Kurz, H. B. E., Streit, T., and S., S., "Investigation of stationary-crossflow-instability induced transition with the temperature-sensitive paint method," *Experimental Thermal and Fluid Science*, Vol. 109, 2019, p. 109848. https://doi.org/https://doi.org/10.1016/j.expthermflusci.2019.109848.

[19] Fey, U., Engler, R., Egami, Y., Iijima, Y., Asai, K., Jansen, U., and Quest, J., "Transition detection by temperature sensitive paint at cryogenic temperatures in the European Transonic Wind tunnel (ETW)," *20th International Congress on Instrumentation in Aerospace Simulation Facilities, 2003. ICIASF'03.*, IEEE, 2003, pp. 77–88.

[20] Saric, W., and Reed, H., "Toward practical laminar flow control-remaining challenges," *2nd AIAA Flow Control Conference*, 2004, p. 2311.

[21] Merino-Martínez, R., Carpio, A. R., Pereira, L. T. L., van Herk, S., Avallone, F., Ragni, D., and Kotsonis, M., "Aeroacoustic design and characterization of the 3D-printed, open-jet, anechoic wind tunnel of Delft University of Technology," *Applied Acoustics*, Vol. 170, 2020, p. 107504.

[22] Rius-Vidales, A. F., Barahona, M., and Kotsonis, M., "Swept Transition Experimental Platform (STEP)," *AIAA Scitech 2024 Forum*, 2024.

[23] Rius-Vidales, A. F., "Influence of a forward-facing step on crossflow instability and transition: An experimental study in a swept wing boundary-layer," Ph.D. thesis, Delft University of Technology, 2022.

[24] Schrader, L.-U., Brandt, L., Mavriplis, C., and Henningson, D. S., "Receptivity to free-stream vorticity of flow past a flat plate with elliptic leading edge," *Journal of Fluid Mechanics*, Vol. 653, 2010, pp. 245–271.

[25] Deyhle, H., and Bippes, H., "Disturbance growth in an unstable three-dimensional boundary layer and its dependence on environmental conditions," *Journal of Fluid Mechanics*, Vol. 316, 1996, p. 73–113. https://doi.org/10.1017/S0022112096000456.

[26] Saric, W., Carrillo, R., Jr, and Reibert, M., "Leading-edge roughness as a transition control mechanism," *36th AIAA aerospace sciences meeting and exhibit*, 1998, p. 781.

[27] Serpieri, J., and Kotsonis, M., "Three-dimensional organisation of primary and secondary crossflow instability," *Journal of Fluid Mechanics*, Vol. 799, 2016, pp. 200–245.

[28] Zoppini, G., Westerbeek, S., Ragni, D., and Kotsonis, M., "Receptivity of crossflow instability to discrete roughness amplitude and location," *Journal of Fluid Mechanics*, Vol. 939, 2022, p. A33.

[29] Tropea, C., Yarin, A. L., Foss, J. F., et al., *Springer handbook of experimental fluid mechanics*, Vol. 1, Springer, 2007.

[30] Örlü, R., and Vinuesa, R., "Thermal anemometry," *Experimental aerodynamics*, CRC Press, 2017, pp. 257–304.

[31] Saric, W. S., Wei, W., and Rasmussen, B. K., "Boundary-layer stability and transition," *Handbook of Experimental Fluid Mechanics*, edited by C. Tropea, A. L. Yarin, and J. F. Foss, Springer, 2007, pp. 886–896.

[32] Liu, Z., "Compressible Falkner–Skan–Cooke boundary layer on a flat plate," *Physics of Fluids*, Vol. 33, No. 12, 2021, p. 126109.

[33] Mack, L. M., "Boundary-layer linear stability theory," Tech. rep., California Inst of Tech Pasadena Jet Propulsion Lab, 1984.

[34] Danabasoglu, G., and Biringen, S., "A Chebyshev matrix method for the spatial modes of the Orr–Sommerfeld equation," *International journal for numerical methods in fluids*, Vol. 11, No. 7, 1990, pp. 1033–1037.

[35] White, F. M., *Viscous fluid flow*, Vol. 3, McGraw-Hill New York, 2006.

[36] Bruun, H. H., *Hot-wire Anemometry: Principles and Signal Analysis*, Oxford University Press, New York, USA, 1995.

[37] Rius-Vidales, A. F., and Kotsonis, M., "Unsteady interaction of crossflow instability with a forward-facing step," *Journal of Fluid Mechanics*, Vol. 939, 2022, p. A19.

[38] White, E. B., and Saric, W. S., "Secondary instability of crossflow vortices," *Journal of Fluid Mechanics*, Vol. 525, 2005, pp. 275–308.

[39] Downs, R. S., and White, E. B., "Free-stream turbulence and the development of cross-flow disturbances," *Journal of Fluid Mechanics*, Vol. 735, 2013, p. 347–380. https://doi.org/10.1017/jfm.2013.484.

[40] Haynes, T. S., and Reed, H. L., "Simulation of swept-wing vortices using nonlinear parabolized stability equations," *Journal of Fluid Mechanics*, Vol. 405, 2000, pp. 325–349.

[41] Wassermann, P., and Kloker, M., "Mechanisms and passive control of crossflow-vortex-induced transition in a three-dimensional boundary layer," *Journal of Fluid Mechanics*, Vol. 456, 2002, pp. 49–84.

[42] Malik, M., Li, F., and Chang, C.-L., "Nonlinear crossflow disturbances and secondary instabilities in swept-wing boundary layers," *IUTAM Symposium on Nonlinear Instability and Transition in Three-Dimensional Boundary Layers: Proceedings of the IUTAM Symposium held in Manchester, UK, 17–20 July 1995*, Springer, 1996, pp. 257–266.

[43] Bonfigli, G., and Kloker, M., "Secondary instability of crossflow vortices: validation of the stability theory by direct numerical simulation," *Journal of fluid mechanics*, Vol. 583, 2007, pp. 229–272.